

# SUPERMASSIVE BLACK HOLE ACCRETION HISTORY INFERRED FROM A LARGE SAMPLE OF *CHANDRA* HARD X-RAY SOURCES

A. J. BARGER,<sup>1,2,3,4</sup> L. L. COWIE,<sup>1,4</sup> M. W. BAUTZ,<sup>5</sup> W. N. BRANDT,<sup>6</sup> G. P. GARMIRE,<sup>6</sup> A. E. HORNSCHEMEIER,<sup>6</sup> R. J. IVISON,<sup>7</sup> F. N. OWEN<sup>8</sup>

*Submitted to the Astronomical Journal*

## ABSTRACT

We describe the optical, near-infrared, and radio properties of a sample of hard (2 – 7 keV) X-ray sources detected in a deep *Chandra* observation of the field surrounding the Abell 370 cluster. We combine these data with similar observations of the *Chandra* Deep Field-North and the Hawaii Survey Field SSA13 to obtain a sample of 69 hard X-ray sources (45 are spectroscopically identified) with extremely deep 20 cm observations. We find that about 4% of the  $> L^*$  galaxy population is X-ray luminous at any time and hence that black hole accretion has a duration of about half a Gyr. We find that about 30% of the summed 2 – 7 keV flux from our total sample is from sources at  $z \lesssim 1$ . We estimate the bolometric luminosities of accretion onto supermassive black holes for our sample, from which we determine maximal mass inflow rates that increase from  $\sim 0.01 M_\odot \text{ yr}^{-1}$  at  $z \lesssim 0.5$  up to  $\sim 10 M_\odot \text{ yr}^{-1}$  at  $z \gtrsim 1$ , assuming a canonical radiative efficiency  $\epsilon \sim 0.1$ . The time history of the *accretion rate density* is evaluated; its maximal integrated value is  $\rho_{BH} = 6 \times 10^{-35} \text{ g cm}^{-2}$ , which is reasonably consistent with the value inferred from the local black hole mass to bulge mass ratio.

*Subject headings:* cosmology: observations — galaxies: distances and redshifts — galaxies: evolution — galaxies: formation — galaxies: active

## 1. INTRODUCTION

X-ray surveys provide a direct probe of active galactic nuclei (AGN) and hence of supermassive black hole accretion activity in the Universe. Soft X-ray samples are biased against sources with high line-of-sight absorption, so it is desirable to observe at the highest possible energies in order to obtain the most complete sample. Two 1 Ms *Chandra* exposures (Brandt et al. 2001b; P. Rosati, et al., in preparation) have essentially fully resolved the X-ray background (XRB) at about  $1.5 \times 10^{-15} \text{ erg cm}^{-2} \text{ s}^{-1}$  in the 2 – 7 keV energy band, and the cumulative counts flatten rapidly below this flux level. The brighter (100–480 ks) *Chandra* (Mushotzky et al. 2000; Giacconi et al. 2001; Hornschemeier et al. 2000, 2001; Brandt et al. 2001a; Garmire et al. 2001; Tozzi et al. 2001) and *XMM-Newton* (e.g., Hasinger et al. 2001) imaging surveys are therefore finding nearly all the hard X-ray sources, and the analysis of these surveys will provide a comprehensive understanding of the nature of the sources that comprise the XRB at these energies.

The excellent  $< 1''$  X-ray positional accuracy of *Chandra* permits the secure identification of the optical counterparts to the X-ray sources. One of the most interesting results obtained from optical follow-up observations is that almost half of the hard X-ray light arises in optically bright galaxies ( $I < 23.5$ ) in the  $z < 1.5$  redshift range. The other half arises in a mixture of higher redshift AGN

and optically faint galaxies ( $I > 23.5$ ), many of whose redshifts likely lie in the range  $z = 1.5$  to 3, based on their colors (Crawford et al. 2001; Barger et al. 2001a; Cowie et al. 2001).

Almost all of the optically bright sources can be spectroscopically identified, and most are bulge-dominated galaxies with near- $L^*$  luminosities. Contrary to the situation for the faint *ROSAT* soft X-ray sources (Schmidt et al. 1998), the vast majority ( $> 85\%$ ) do not have broad optical or ultraviolet lines, and about half of the optically identified sources show no obvious high ionization signatures of AGN activity. The *Chandra* hard X-ray sources prior to the 1 Ms data are generally too faint to allow the multiparameter fits to the X-ray spectra that would directly measure the intrinsic column densities. However, the soft to hard X-ray flux ratios suggest that the sources are highly absorbed systems whose high column densities could effectively extinguish the optical, ultraviolet, and near-infrared continua from the AGN and render traditional identification techniques ineffective.

One of the most exciting avenues in the study of the hard X-ray source populations is determining the times and duration of distant supermassive black hole activity. Barger et al. (2001a) found that about 7% of optically luminous galaxies are X-ray active at any time. A similar active fraction (6%) was later found by Hornschemeier et al. (2001) for the 225 ks *Chandra* Deep Field-North (CDF-

<sup>1</sup>Institute for Astronomy, University of Hawaii, 2680 Woodlawn Drive, Honolulu, Hawaii 96822

<sup>2</sup>Department of Astronomy, University of Wisconsin-Madison, 475 North Charter Street, Madison, WI 53706

<sup>3</sup>Hubble Fellow and Chandra Fellow at Large

<sup>4</sup>Visiting Astronomer, W. M. Keck Observatory, jointly operated by the California Institute of Technology and the University of California

<sup>5</sup>Center for Space Research, Massachusetts Institute of Technology, Cambridge, MA 02139

<sup>6</sup>Department of Astronomy and Astrophysics, 525 Davey Laboratory, The Pennsylvania State University, University Park, PA 16802

<sup>7</sup>UK Astronomy Technology Centre, Royal Observatory, Blackford Hill, Edinburgh EH9 3HJ, U.K.

<sup>8</sup>National Radio Astronomy Observatory, P.O. Box O, 1003 Lopezville Road, Socorro, N.M. 87801

N) data. Thus, these studies suggest that, on average, accretion activity lasts for on order of half a Gyr over the lifetime of a galaxy.

In this paper we present a multiwavelength study of the hard X-ray sources detected in the field containing the  $z = 0.37$  massive lensing cluster A370 (Bautz et al. 2000), the SSA13 field (Mushotzky et al. 2000; Barger et al. 2001a, hereafter B01), and the CDF-N field (Hornschemeier et al. 2001, hereafter H01).

Bautz et al. (2000) presented the detection in hard X-rays of the two distant submillimeter sources at  $z = 2.80$  and  $z = 1.06$  behind the A370 cluster; these sources are gravitationally amplified by factors of 2.4 and 2.1, respectively. The remaining 13 hard X-ray sources are not strongly affected either by the cluster lens (amplifications between 1 and 1.3) or by the diffuse emission from the cluster. In the following analysis we take into account the two large amplifications but neglect the smaller amplifications, treating the remaining objects as a field sample.

When we combine the A370 data with the SSA13 and CDF-N data, we obtain a sample of 69 hard X-ray selected sources with extremely deep 20 cm and optical imaging data. We have spectroscopic redshifts for 45 of the 69 sources. We use our combined sample to determine the optical properties of the X-ray sources that comprise the hard XRB, the duty cycle of X-ray activity, and the luminosities associated with AGN accretion. We then evaluate the mass inflow rate onto the supermassive black holes and deduce the time history of the accretion rate density.

We take  $H_o = 65 h_{65} \text{ km s}^{-1} \text{ Mpc}^{-1}$  and use an  $\Omega_M = 1/3$ ,  $\Omega_\Lambda = 2/3$  cosmology throughout.

## 2. A370 SAMPLE AND OBSERVATIONS

### 2.1. *X-ray Observations*

*Chandra* observed A370 on 22–23 October 1999 for a total of 93.7 ks with the ACIS S3 detector. The telescope optical axis was pointed approximately 2.4' E of the cluster center. The ACIS focal plane temperature during the observation was  $-110^\circ \text{ C}$ . The detectors were read out in timed-exposure mode and events were processed on board in faint mode. The (re)processed data were delivered by the *Chandra* X-ray Observatory Center (CXC) on 4 September 2000.

We processed the Level 2 CXC data products using standard methods. Periods of background flaring were removed using the tool `lc_clean` developed by Maxim Markevitch. The total S3 counting rate (0.1 to 10 keV) was measured in 100 s time bins, and a quiescent background of  $1.59 \text{ counts s}^{-1}$  (over the full S3 detector) was estimated from one 17 ks period. Time bins in which the observed background differed from the quiescent value by more than  $2.3\sigma$  were excluded from our subsequent analysis. The net flare-free exposure time was 63.2 ks.

We restrict attention to events occurring in the S3 detector with *ASCA* grades 0, 2, 3, 4, and 6 and with energies between 0.3 and 7 keV in order to maximize the signal-to-noise ratio. The  $0.3 - 7 \text{ keV}$  background level in source-free regions of the field is  $(2.09 \pm 0.02) \times 10^{-6} \text{ counts s}^{-1} \text{ arcsec}^{-2}$ .

We used the CIAO tool `wavdetect`, with a significance parameter value of  $10^{-7}$ , to search for sources in the  $0.5 - 7 \text{ keV}$ ,  $0.5 - 2 \text{ keV}$ , and  $2 - 7 \text{ keV}$  bands. A to-

tal of 34, 25, and 17 sources, respectively, were detected in each band. The expected false detection rate in each band is 0.1 source. We selected all sources that were more than  $15''$  from the chip edges; this removed one soft and hard band source from the `wavdetect` sample. The individual soft and hard band sources were then reviewed and compared with the results of a cell detection method. Two hard band sources detected by `wavdetect` had only 5 counts each. One of these sources could not be reproduced with the cell detection method and was removed. The other source was measured to have 8.3 counts in a  $2''$  radius aperture. For this source we have used the counts determined by the aperture photometry; it is marked in Table 1. Subsequent work on the 1 Ms CDF-N data has shown that `wavdetect` detections with a significance parameter of  $10^{-7}$  are highly reliable (see §3.2.3 of Brandt et al. 2001b), but, for the present paper, we have chosen to remain with our initial sample selection. We are left with a total of 15 hard X-ray sources in our A370 sample.

We converted the detected counts for each source into fluxes assuming a photon spectral flux distribution function  $\frac{dN}{dE} \propto E^{-\Gamma}$ , modified by the expected Galactic absorbing column density of  $4.0 \times 10^{20} \text{ cm}^{-2}$ , assuming an intrinsic  $\Gamma = 2$ . In creating exposure maps to account for energy-dependent vignetting and detector efficiency variations using the CIAO tools `mkinstmap` and `mkexppmap`, we also assumed  $\Gamma = 2$ . Since the fluxes in the SSA13 and CDF-N fields were analyzed with a harder  $\Gamma$  ( $\Gamma = 1.2$  was the counts-weighted mean photon index for the SSA13 sample, and  $\Gamma = 1.4$  was assumed for sources in the CDF-N sample when the individual  $\Gamma$ s could not be determined), we repeated the counts-to-flux conversion procedure on our A370 sample using  $\Gamma = 1.2$ . We found that soft band fluxes increased by 25% and hard band fluxes increased by 33%. To be more consistent with the SSA13 and CDF-N samples, we adopt these correction factors in our subsequent analysis.

Ten of the 34 sources detected in the broad-band image with `wavdetect` coincide within  $2''$  with radio sources detected at high significance with the VLA (see §2.4). The mean position offsets (*Chandra* – VLA) for these sources are  $0.4''$  and  $0.0''$  in right ascension and declination, respectively. The dispersion of the positions is  $0.55''$ . We have corrected the positions in the tables to allow for this small offset.

Figure 1 shows the *Chandra*  $2 - 7 \text{ keV}$  image of A370 with the final 15 hard X-ray source positions identified by small circles. Table 1 details these 15 sources, ordered by increasing RA. The first five columns in Table 1 include the source identification, RA(2000), Dec(2000),  $2 - 7 \text{ keV}$  flux, and  $0.5 - 2 \text{ keV}$  flux. Table 2 details the supplementary 14 sources in our field that were not detected in the hard band but were detected in the soft band. The first four columns include the source identification, RA(2000), Dec(2000), and  $0.5 - 2 \text{ keV}$  flux. The remaining entries in the tables are discussed in subsequent sections.

### 2.2. *Optical and Near-Infrared Imaging*

Deep multicolor images ( $V, R, I$ ) that cover the A370 *Chandra* field were obtained using the Low-Resolution Imaging Spectrometer (LRIS; Oke et al. 1995) on the Keck 10 m telescopes. Wide-field near-infrared images were obtained with the UH 2.2 m telescope using the University

of Hawaii Quick Infrared Camera (QUIRC; Hodapp et al. 1996) and a notched  $HK'$  ( $1.9 \pm 0.4 \mu\text{m}$ ) filter. Details of the observations can be found in Cowie et al. (2001) and E. Hu, L. Cowie, & R. McMahon, in preparation.

Figure 2 shows thumbnail  $I$ -band images of the 15 hard X-ray sources listed in Table 1. In selecting the optical counterparts, we considered only sources within a  $1.5''$  radius of the nominal X-ray position. The optical separations are given in column 11 of Table 1. The magnitudes were measured in  $3''$  diameter apertures at the optical center and corrected to approximate total magnitudes using an average offset (Cowie et al. 1994); henceforth, we refer to these as corrected  $3''$  diameter apertures. The  $HK'$ ,  $I$ ,  $R$ , and  $V$  magnitudes are given in columns 6–9 of Table 1. The  $2\sigma$  limits are approximately  $HK' = 20.9$ ,  $I = 24.9$ ,  $R = 26.1$ , and  $V = 26.1$ . All of the sources have identifications in the  $I$  band, and none of the counterparts are fainter than  $I = 23.5$ , which was found to be the effective optical limit for spectroscopic identification of the sources in the SSA13 hard X-ray sample (B01).

### 2.3. Keck Spectroscopy

We made spectroscopic observations of the X-ray sources in the A370 field using LRIS slit-masks on the Keck 10 m telescope on UT 2000 February 6 and 2001 January 23–24. We positioned the slit at the center of the optical counterpart. We used  $1.4''$  wide slits. In the February run we used the 300 lines  $\text{mm}^{-1}$  grating blazed at  $5000 \text{ \AA}$ , which gives a wavelength resolution of approximately  $16 \text{ \AA}$  and a wavelength coverage of approximately  $5000 \text{ \AA}$ . The wavelength range for each object depends on the exact location of the slit in the mask but is generally between  $\sim 5000$  and  $10000 \text{ \AA}$ . In the January run we used either the 400 lines  $\text{mm}^{-1}$  grating blazed at  $8500 \text{ \AA}$ , which gives a wavelength resolution of approximately  $12 \text{ \AA}$  and a wavelength coverage of approximately  $4000 \text{ \AA}$ , or the 600 lines  $\text{mm}^{-1}$  grating blazed at  $10000 \text{ \AA}$ , which gives a wavelength resolution of approximately  $8 \text{ \AA}$  and a wavelength coverage of approximately  $2500 \text{ \AA}$ . We used the D560 dichroic to obtain simultaneous LRIS-B observations with the 600 lines  $\text{mm}^{-1}$  grism blazed at  $5000 \text{ \AA}$ , which for our slit width gives a wavelength resolution of approximately  $7 \text{ \AA}$  and a wavelength coverage of approximately  $2000 \text{ \AA}$ .

Each slit mask was observed for 1.5 hr, broken into three sets of 0.5 hr exposures. Fainter objects were put in more than one mask to provide longer total exposures. Conditions were photometric with seeing  $\sim 0.6'' - 0.8''$  FWHM. The objects were stepped along the slit by  $2''$  in each direction, and the sky backgrounds were removed using the median of the images to avoid the difficult and time-consuming problems of flat-fielding LRIS data. Details of the spectroscopic reduction procedures can be found in Cowie et al. (1996).

We successfully obtained redshift identifications for 10 of the 15 hard X-ray sources in our sample. Two others were already identified in the literature: source 12 from Ivison et al. (1998) and source 11 from Barger et al. (1999b) and Soucail et al. (1999). The spectra for the hard X-ray sources (except source 12) are shown in Fig. 3, and the redshifts are given in column 10 of Table 1. Strong emission line features are marked on the plots. We also obtained redshift identifications for 8 of the 14 additional soft X-

ray sources in the field, and these are given in column 5 of Table 2.

### 2.4. Radio Observations

A very deep 1.4 GHz map of the A370 field was obtained by F. Owen, et al., in preparation, with the National Radio Astronomy Observatory's Very Large Array (VLA). The data comprise 45 hr in A configuration and 20 hr in B configuration, using the spectral-line correlator mode together with short integration times to eliminate bandwidth smearing. A large field-of-view ( $40'$  in diameter) was completely imaged. In the region covered by the *Chandra* results reported here, the effective resolution is 1.6 arcseconds and the rms noise is typically  $5.5 - 6.5 \mu\text{Jy}$ , depending on details of the residual sidelobe distribution from nearby sources; thus, we have adopted  $20 \mu\text{Jy}$  as a  $3\sigma$  upper limit for undetected sources. The radio fluxes were measured at the highest peak within  $2''$  of each X-ray position; these fluxes are given in column 12 of Table 1 and column 6 of Table 2.

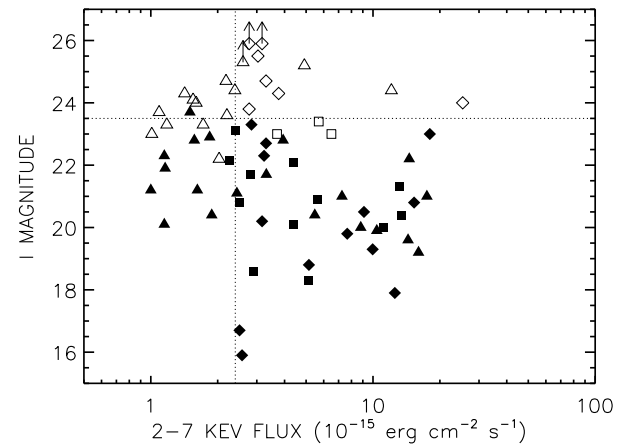


FIG. 4.—  $I$  magnitude versus 2–7 keV flux for the hard X-ray sources in the A370 (squares), CDF-N (triangles), and SSA13 (diamonds) fields. Sources with spectroscopic identifications are denoted by filled symbols. The horizontal dotted line at  $I = 23.5$  indicates our magnitude division between optically faint and optically bright galaxies; all but seven of the sources brighter than this limit have spectroscopic identifications. The dotted vertical line at  $2.4 \times 10^{-15} \text{ erg cm}^{-2} \text{ s}^{-1}$  is the hard X-ray detection limit for the A370 and the SSA13 samples. The hard X-ray flux of one of the sources in the A370 field (source 12) is fainter than the hard X-ray detection limit after correcting for cluster magnification.

### 3. COMBINED A370, CDF-N, AND SSA13 DATASETS

We hereafter use a combined hard X-ray sample from the A370, CDF-N, and SSA13 fields. In order to merge the samples we converted the 2–10 keV fluxes from B01 and the 2–8 keV fluxes from H01 to the 2–7 keV band using  $\Gamma = 1.2$ . The X-ray detection limit for the A370 and SSA13 samples is  $2.4 \times 10^{-15} \text{ erg cm}^{-2} \text{ s}^{-1}$  (2–7 keV), and the detection limit for the CDF-N sample is  $5.6 \times 10^{-16} \text{ erg cm}^{-2} \text{ s}^{-1}$  (2–7 keV). For the present work we have restricted the CDF-N sample to sources with fluxes greater than  $1.0 \times 10^{-15} \text{ erg cm}^{-2} \text{ s}^{-1}$  (2–7 keV) to provide a conservative sample with uniform flux selection over the field area. This CDF-N sample, adapted from H01, is given in Table 3. We include in the table  $HK'$

and  $B$ -band magnitudes from Barger et al. (1999a) and A. Barger, et al., in preparation, respectively. We also include 20 cm data from Richards et al. (2000). The combined sample consists of 69 sources with 2–7 keV fluxes ranging from  $1.0 \times 10^{-15}$  erg cm $^{-2}$  s $^{-1}$  to  $2.5 \times 10^{-14}$  erg cm $^{-2}$  s $^{-1}$ .

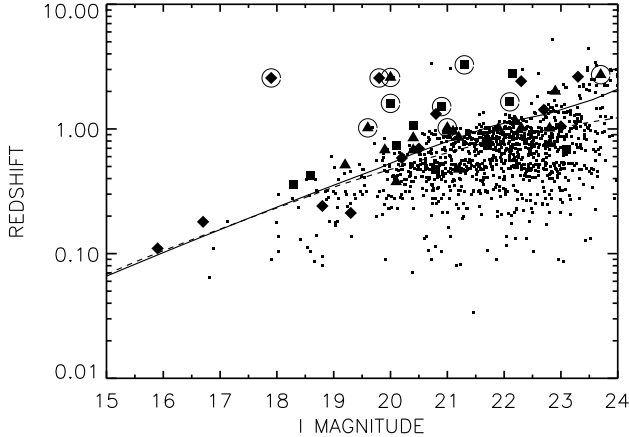


FIG. 5.— Redshift versus  $I$  magnitude for the 45 hard X-ray sources with spectroscopic identifications in the A370 (squares), CDF-N (triangles), and SSA13 (diamonds) fields and for an  $I < 24$  field galaxy sample from the CDF-N, SSA13, and SSA22 (small symbols) fields. Superimposed are Coleman, Wu, & Weedman (1980) evolved tracks for an early-type galaxy (solid) and an irregular galaxy (dashed) with  $M_I = -22.5$ . Sources with broad emission lines are circled.

#### 4. OPTICAL PROPERTIES OF THE COMBINED HARD X-RAY SAMPLES

##### 4.1. Magnitudes

In Fig. 4 we plot  $I$  magnitude versus 2–7 keV flux for the combined sample. The filled symbols denote sources with spectroscopic identifications; 45 of the 69 sources (65%) have redshift identifications, and all but seven of the sources brighter than  $I = 23.5$  (as indicated by the horizontal line) have redshifts. The three samples are very similar in their distribution of optical magnitudes and redshift identifications.

The median and mean  $I$  magnitudes as a function of hard X-ray flux are summarized in Table 4. As has been noted previously (e.g., H01), the data are consistent with a constant optical to hard X-ray ratio, though there is a very wide range of optical magnitudes for a given X-ray flux.

In Fig. 5 we plot redshift versus  $I$  magnitude for the 45 spectroscopically identified hard X-ray sources in the combined sample (large symbols). For comparison, we include on the figure an optically selected  $I < 24$  field galaxy sample (small symbols). We superimpose on the figure tracks calculated from the spectral energy distributions (SEDs) of Coleman, Wu, & Weedman (1980) for an early-type galaxy (solid) and an irregular galaxy (dashed) in the absence of evolution, both with absolute magnitude  $M_I = -22.5$  in the assumed cosmology. B01 noted that the hard X-ray sources predominantly lie in the most optically luminous galaxies, and as Fig. 5 shows, this is also the case for the combined sample. Brandt et al. (2001a) have recently noted that this property appears to continue to hold to fainter X-ray flux levels,  $\sim 3 \times 10^{-16}$  erg cm $^{-2}$  s $^{-1}$ .

We have circled the sources with broad emission lines in their spectra. These sources tend to lie to the left of the evolved galaxy tracks for a given redshift, indicating substantial optical brightening due to the AGN's optical emission.

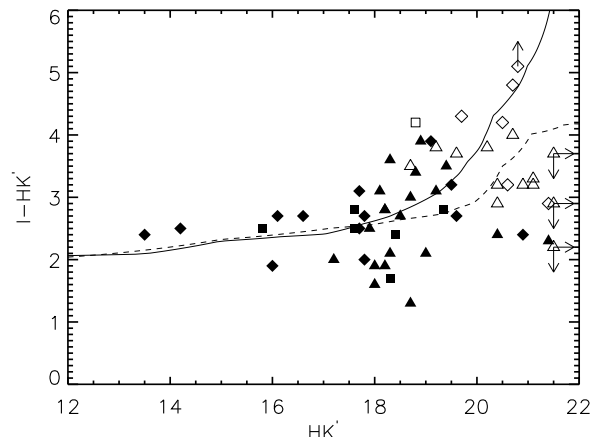
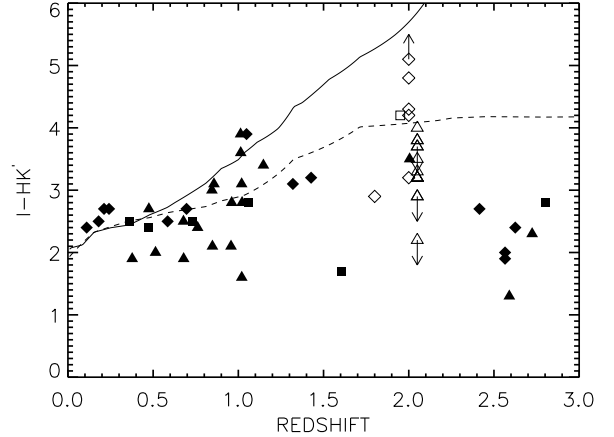


FIG. 6.— (a)  $I - HK'$  color versus redshift and (b)  $I - HK'$  color versus  $HK'$  magnitude for the hard X-ray sources in the A370 (squares), CDF-N (triangles), and SSA13 (diamonds) fields with optical and/or near-infrared detections (two sources — one in the CDF-N field and one in the SSA13 field — with only limits on both magnitudes are not shown). The spectroscopically unidentified sources are nominally placed at  $z = 2$  (slight redshift offsets have been applied to allow the three fields to be distinguished). The source from the SSA13 field that has a millimetric redshift of 1.8 (as deduced from the submillimeter to radio flux ratio; see B01) is shown as an open diamond in (a) at  $z = 1.8$ . The overlays are Coleman, Wu, & Weedman (1980) tracks for an early-type galaxy (solid curve) and a spiral galaxy (dashed curve) with  $M_{HK'} = -25.0$ .

##### 4.2. Optical Spectral Classification

Following B01, we classify the optical spectra of the hard X-ray sources into three general categories: (i) broad emission lines, (ii) clear signs of [NeIII] and/or [NeV] and/or CIV, and (iii) no sign of any of the above signatures. The spectra are generally of high quality, and strong high ionization lines are easily seen. We have included four new redshifts in the CDF-N sample (sources 9, 13, 15, and 30); these spectra will be presented in a forthcoming paper (A. Barger, et al., in preparation). We measured all but three of the redshifts in Table 3 from our own Keck LRIS spec-

tra. The redshifts of the three sources in our table for which we do not have Keck spectra (sources 22, 25, and 26) are taken from the compilation in H01 (the first two were measured by H01 from Hobby-Eberly Telescope spectra, and the last one was measured by Cohen et al. (2000) from a Keck LRIS spectrum.) Table 5 gives the numbers of sources in each of the three optical spectral classes for each sample. The identified fractions across the samples are divided fairly evenly into sources that show broad or high ionization lines in their optical spectra and sources that show no such optical signatures.

#### 4.3. Colors

In Fig. 6a we plot  $I - HK'$  color versus redshift for sources in the combined sample with measured  $HK'$  and  $I$  magnitudes or limits and spectroscopic identifications (filled symbols). We place sources without spectroscopic identifications at  $z = 2$  and identify them with open symbols. In Fig. 6b we plot  $I - HK'$  versus  $HK'$  for sources with measured  $HK'$  and  $I$  magnitudes or limits. The overlays are Coleman, Wu, & Weedman (1980) tracks for a non-evolving early-type galaxy (solid curve) and a spiral galaxy (dashed curve) with  $M_{HK'} = -25.0$ . The colors of most of the spectroscopically identified  $z < 1.5$  galaxies are in the range of the galaxy tracks. A sizeable fraction of the spectroscopically unidentified sources have colors that are consistent with luminous galaxies at  $z > 1.5$ .

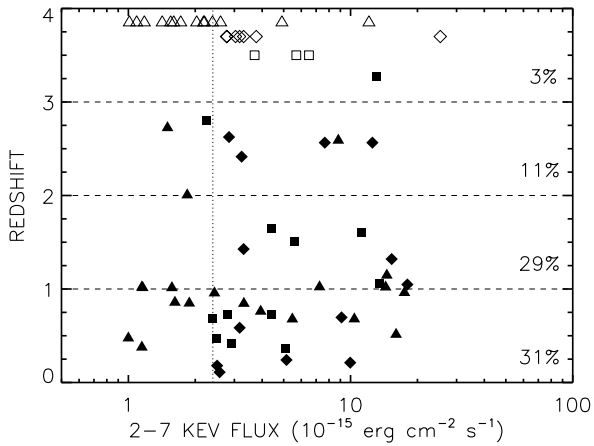


FIG. 7.— Redshift versus 2–7 keV flux for the hard X-ray sources in the A370 (squares), CDF-N (triangles), and SSA13 (diamonds) fields. Sources with spectroscopic identifications are denoted by filled symbols. The dotted vertical line at  $2.4 \times 10^{-15}$  erg  $\text{cm}^{-2} \text{s}^{-1}$  is the hard X-ray detection limit for the A370 and SSA13 samples. The dashed horizontal lines separate the sources into redshift bins. The percentages indicate how much hard X-ray flux originates in each redshift bin relative to the total flux in our sample. Spectroscopically unidentified sources are arbitrarily plotted at the top of the figure and are not included in the listed percentage contributions; many are likely to lie in the redshift range  $z = 1.5$  to 3.

#### 4.4. Redshift Distribution

We show the redshift distribution of the sources versus hard X-ray flux in Fig. 7, where we also give the percentage of the hard X-ray flux originating in each redshift interval relative to the total flux in our sample. Figure 7 shows that about 30% of the summed hard X-ray flux from all of our sources has occurred since  $z = 1$ , when the Universe

was half its present age. The spectroscopically unidentified sources (which are most likely to lie in the redshift range  $z = 1.5$  to  $z = 3$ ) are not included in the percentages given, but the spectroscopically identified sources already make up about three-quarters of the summed hard X-ray flux in our sample.

#### 5. THE DUTY CYCLE OF X-RAY ACTIVITY

The *Chandra* data allow us to estimate the duty cycle of X-ray activity in galaxies. Spectroscopically identified hard X-ray sources are common in bulge-dominated (see thumbnail images in Fig. 2; see also Fig. 2 of B01 and Fig. 6 of H01) optically luminous galaxies (see Fig. 5). In B01 we measured the X-ray properties of known luminous galaxies in an optically selected field galaxy sample and found that  $7^{+5}_{-3}\%$  were X-ray active.

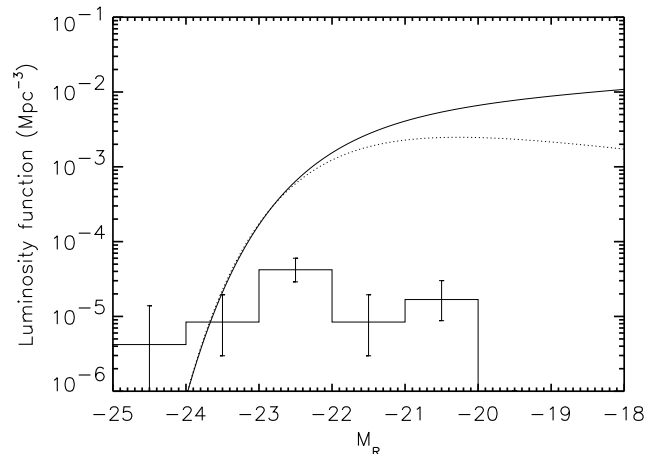


FIG. 8.—  $R$ -band luminosity function from the  $z = 0 - 1$  combined hard X-ray selected sample (histogram; uncertainties are  $1\sigma$ ). The local  $R$ -band luminosity functions of Lin et al. (1996; dotted line) and Geller et al. (1997; solid line) are shown for comparison.

Here we adopt a different approach: we construct the optical luminosity function (LF) of our X-ray selected sample and compare it with the local LF. The optical LF of red galaxies is relatively invariant over the  $z = 0$  to 1 redshift range (Lilly et al. 1995). In order to make the most direct comparison, we have chosen to construct an  $R$ -band LF using our  $z = 0 - 1$  hard X-ray selected sample. In cases where we do not have a measured  $R$ -band magnitude for a galaxy, we have estimated the  $R$  magnitude using an average  $R - I = 0.6$  color (measured from galaxies in the CDF-N) and the galaxy's  $I$  magnitude. In computing the absolute rest-frame magnitudes,  $M_R$ , we have used K-corrections appropriate for an Sb galaxy.

We first made a histogram of the absolute rest-frame magnitudes and then divided the numbers in the bins by the  $z = 0 - 1$  comoving volume. Figure 8 shows the result and a comparison with the local  $R$ -band LFs of Lin et al. (1996) and Geller et al. (1997) (the parameters for both were taken from the compilation by Geller et al.) The LF is X-ray flux selected and would increase slowly as the flux selection was decreased below  $1.0 \times 10^{-15}$  erg  $\text{cm}^{-2} \text{s}^{-1}$ , but this effect may be expected to be small because the cumulative counts converge rapidly below this flux limit. Formally, the current X-ray selected LF is a lower bound to the luminosity density of galaxies showing X-ray activity.

If we integrate the local LFs and our histogram above  $L^*$  (with  $H_o = 65 \text{ km s}^{-1} \text{ Mpc}^{-1}$ ,  $M^* = -21.66$  for Geller et al. and  $M^* = -21.58$  for Lin et al.), we find that  $4 \pm 1\%$  of the galaxies are X-ray active. If we extend the integral down to  $0.5 L^*$ , the percentage is  $1.5 \pm 0.5\%$  using Geller et al. and  $2 \pm 0.5\%$  using Lin et al.

If the fraction of  $> L^*$  galaxies showing such behavior reflects the fraction of time that each galaxy spends accreting onto its supermassive black hole, then each such galaxy must be active for about half a Gyr. The duration of X-ray activity is much longer than the theoretically estimated accretion time of 0.01 Gyr for black hole fuelling by a merger (Kauffmann & Haenelt 2000) and may suggest that the accretion is being powered by many small mergers or by internal flows within the galaxies, at least in the  $z = 0 - 1$  redshift range.

## 6. BOLOMETRIC LUMINOSITIES

Following B01, we use our multiwavelength dataset to estimate bolometric luminosities ( $L_{BOL} = L_{FIR} + L_{OPT} + L_X$ ) for our combined hard X-ray selected sample. For the spectroscopically unidentified sources, we nominally assume  $z = 2$ .

As in § 3.3 of B01, we allow for the average effects of opacity in the calculation of our hard X-ray luminosities by normalizing the flux at 4 keV for a  $\Gamma = 2$  spectrum to the flux at 4 keV calculated over the 2 – 7 keV energy range for a spectrum with photon index  $\Gamma = 1.2$ . Then

$$L_{HX} = 4 \pi d_L^2 f_{HX} \quad (1)$$

where  $f_{HX}$  is the 2 – 7 keV flux of Table 1 and Table 3. For this energy range the  $L_{HX}$  equation would be the same if we had instead used  $\Gamma = 1.4$ . The inferred hard X-ray luminosities for the sources in the A370 and CDF-N fields are given in column 3 of Table 6.

The total X-ray luminosity is only weakly sensitive to the adopted energy range for a photon index  $\Gamma = 2$ . For an energy range from 0.1 to 100 keV, the ratio of the total X-ray luminosity,  $L_X$ , to the 2 – 7 keV luminosity is  $\ln(1000)/\ln(3.5) = 5.5$ . The total X-ray luminosities of the sources are smaller than the contributions to the bolometric luminosities from other wavelengths.

We estimate the luminosities in the ultraviolet/optical using the equation given in § 4.3 of B01,

$$L_{OPT} = 4 \pi d_L^2 (9.4 \times 10^{15}) f_{2500(1+z)} (1+z)^{-1} \quad (2)$$

where  $d_L$  is the luminosity distance in cm and  $f_{2500(1+z)}$  has units  $\text{erg cm}^{-2} \text{ s}^{-1} \text{ Hz}^{-1}$ . For the CDF-N sample,  $f_{2500(1+z)}$  is interpolated from the observed fluxes that correspond to the magnitudes given in Table 3, and, where available, the measured  $R$  magnitudes from H01 and the  $U'$  (3400Å) magnitudes from G. Wilson, et al., in preparation. For sources that have substantial galaxy light contamination,  $L_{OPT}$  is an upper limit on the AGN contribution in the ultraviolet/optical.

For the A370 field, where we have substantially less imaging data, we have only been able to calculate  $L_{OPT}$  for the five sources in Table 1 with sufficient magnitude coverage — given the measured or assumed redshifts — to allow reliable interpolations (sources 3, 4, 5, 6, and

12). The inferred bolometric ultraviolet/optical luminosities for the A370 and CDF-N sources are listed in column 4 of Table 6.

The bolometric far-infrared (FIR) flux is related to the rest-frame 20 cm flux through the well-established FIR-radio correlation (Condon 1992) of local starburst galaxies and radio-quiet AGN. The correlation also seems to hold at high redshift (e.g., Carilli & Yun 2000; Barger, Cowie, & Richards 2000). It is not entirely known what mechanism produces the relationship. In galaxies without a powerful AGN, the radio luminosity is dominated by diffuse synchrotron emission; thus, the tight empirical correlation is thought to be a consequence of the radio continuum emission and the thermal dust emission both being linearly related to the massive star formation rate. In the present systems a substantial fraction of the FIR luminosity may also be of AGN origin rather than from star formation, but the only strong statement that we can make is that the FIR luminosity from the AGN is bounded above by the FIR-radio correlation result from §6.3 of B01,

$$L_{FIR} = 4 \pi d_L^2 (8.4 \times 10^{14}) f_{20} (1+z)^{-0.2} \quad (3)$$

Here  $d_L$  is in cm and  $f_{20}$  has units  $\text{erg cm}^{-2} \text{ s}^{-1} \text{ Hz}^{-1}$ .

The inferred bolometric FIR luminosities or limits for the hard X-ray sources in the A370 and CDF-N fields are given in column 5 of Table 6. The luminosities for the sources that are not detected above the radio  $3\sigma$  limit are calculated as upper limits based on the  $3\sigma$  limit. The SSA13 hard X-ray, optical, and FIR luminosities can be found in Table 2 of B01.

In Fig. 9 we plot the ratios  $L_{FIR}/L_{HX}$  (open symbols) and  $L_{OPT}/L_{HX}$  (filled symbols) versus redshift for the spectroscopically identified sources for which we were able to estimate  $L_{OPT}$ . The FIR light dominates over the optical light in a high fraction (73%) of the sources. For the sources in the A370 field for which we were unable to estimate  $L_{OPT}$ , we take  $L_{FIR}$  to be the upper limit to the bolometric luminosity. For all sources we are neglecting possible contributions in the extreme ultraviolet, for which we do not have data.

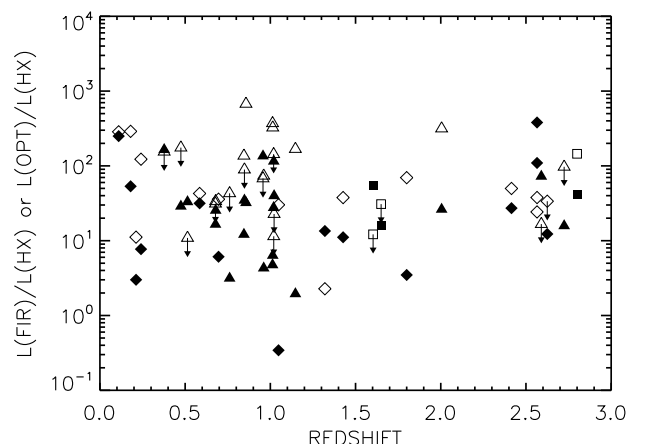


FIG. 9.— Ratio of the bolometric optical (filled) and radio inferred FIR (open) luminosities to the hard X-ray luminosities versus redshift for the A370 (squares), CDF-N (triangles), and SSA13 (diamonds) fields. Spectroscopically unidentified sources are not shown. Downward pointing arrows indicate the use of  $3\sigma$  radio limits in estimating the FIR luminosities.

## 7. ACCRETION HISTORY

The mass inflow rate into a black hole,  $dM/dt$  or  $\dot{M}_{BH}$ , is related to the AGN's bolometric luminosity by  $\epsilon\dot{M}_{BH} = L_{BOL}/c^2$ , where  $\epsilon$  is the radiative efficiency of the accretion energy. With  $\dot{M}_{BH}$  in units of  $M_\odot \text{ Gyr}^{-1}$ , the relation is

$$\dot{M}_{BH} = 1.76 \times 10^5 (0.1/\epsilon) (L_{BOL}/10^{42}) \quad (4)$$

where  $L_{BOL}$  is in units of  $\text{erg s}^{-1}$ .

If we make the simplifying assumption that  $\epsilon$  has an approximately universal value,  $\epsilon \sim 0.1$ , we can evaluate  $\dot{M}_{BH}$  for our hard X-ray sources. We calculate  $\dot{M}_{BH}$  upper bounds from our estimated values of  $L_{BOL}$  (§6) and lower bounds with  $L_{BOL}$  replaced by  $L_X$ .

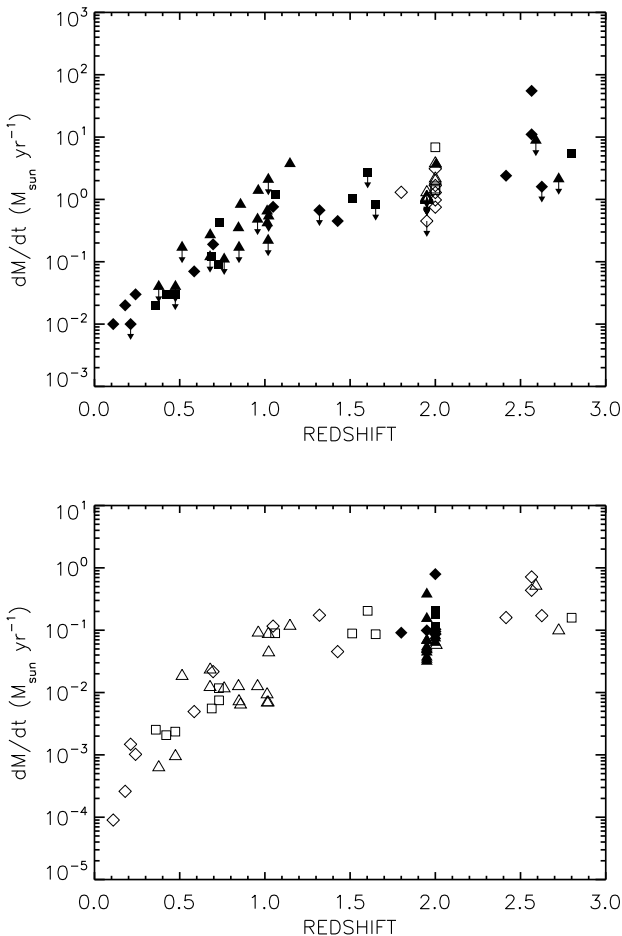


FIG. 10.— The mass inflow rate ( $dM_{BH}/dt$  or  $\dot{M}_{BH}$ ) versus redshift for the hard X-ray sources in the A370 (squares), CDF-N (triangles), and SSA13 (diamonds) fields calculated using either (a) the bolometric luminosities,  $L_{BOL}$ , or (b) the bolometric X-ray luminosities,  $L_X$ . Downward pointing arrows in (a) indicate the use of  $3\sigma$  radio limits in calculating the FIR luminosities. In (a), spectroscopically identified sources are denoted by filled symbols and spectroscopically unidentified sources are denoted by open symbols, nominally placed at  $z = 2$  (a slight offset in redshift has been applied to the unidentified sources with radio limits). In (b), we invert the above for contrast, such that the spectroscopically identified sources are denoted by open symbols, and the spectroscopically unidentified sources are denoted by filled symbols. The source in the SSA13 field with a millimetric redshift of 1.8 (as deduced from the submillimeter to radio flux ratio; see B01) is shown as a diamond at  $z = 1.8$ .

Figure 10 shows the  $\dot{M}_{BH}$  values versus redshift for the canonical  $\epsilon = 0.1$ . The upper bounds in Fig. 10a are on average about a factor 20 higher than the lower bounds in Fig. 10b, but the trends with redshift discussed below are similar for both. To generate a  $10^9 M_\odot$  black hole over an accretion period of order 0.5 Gyr, an  $\dot{M}$  of the order of  $2 M_\odot \text{ yr}^{-1}$  is required.

The lower envelope of the  $\dot{M}_{BH}$  versus redshift plot simply reflects selection bias, since high redshift sources with low  $\dot{M}_{BH}$  will not be detected in the current hard X-ray surveys. The upper envelope of the distribution strongly reflects the changing strength of the maximal accretion rate with redshift, although some of the change is due to the volume increase with redshift, which gives a higher chance of finding very luminous sources ( $\Delta V$  for a  $z = 2-3$  bin is a factor 3.3 larger than for a  $z = 0-1$  bin). At  $z \gtrsim 1$  the inferred accretion rates are up to two orders of magnitude larger than those at  $z \lesssim 0.5$ . Thus, the most violent episodes of black hole growth occurred at early times. For  $z \lesssim 1$ ,  $\log(\dot{M}_{BH})$  increases approximately linearly with redshift. If the *Chandra* surveys are still missing AGN that suffer from Compton thick absorption, then these sources would selectively appear at lower redshifts since the effective column density is a factor of  $(1+z)^{2.6}$  lower than the true column density (B01).

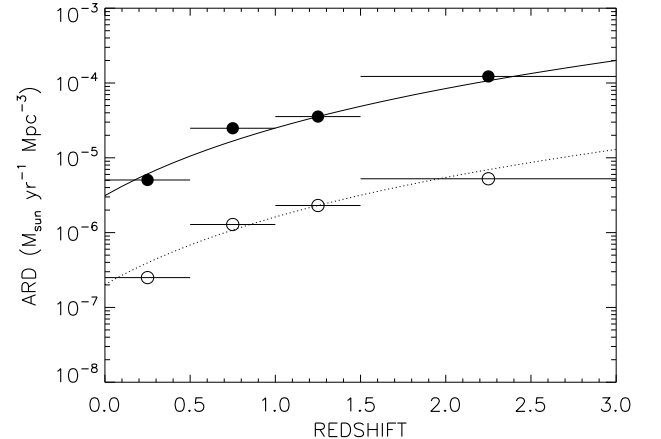


FIG. 11.— The accretion rate density ( $d\rho_{BH}/dt$  or  $\dot{\rho}_{BH}$ ) of the combined hard X-ray sample versus redshift for four redshift bins:  $0 < z < 0.5$ ,  $0.5 \leq z < 1$ ,  $1 \leq z < 1.5$ , and  $1.5 \leq z \leq 3$ . The solid data points are calculated from the bolometric luminosities, and the open data points are calculated from the bolometric X-ray luminosities. The curves illustrate a  $(1+z)^3$  dependence, normalized to the  $1 \leq z < 1.5$  redshift bin.

From the  $\dot{M}_{BH}$  versus redshift distribution, we can deduce the time history of the accretion rate density (ARD),  $\dot{\rho}_{BH} = \sum \dot{M}_{BH}/\Delta V$ , where the sum is over the sources in a bin  $\Delta z$  and  $\Delta V$  is the comoving volume element in  $\text{Mpc}^3$ , which is proportional to the area coverage. The A370, CDF-N, and SSA13 fields have areas of 56, 78, and 64  $\text{arcmin}^2$ , respectively, giving a total area  $A = 198 \text{ arcmin}^2$ . The maximal and minimal results for the ARD history, determined from the upper and lower bounds of Fig. 10, are given in Fig. 11. Again, this is normalized with a value of  $\epsilon \sim 0.1$ , and the accretion rates scale as  $\epsilon^{-1}$ .

The time history of the ARD seems to fall roughly as

$(1+z)^3$ , as illustrated by the overlaid curves in Fig. 11, although the evolution could be slower considering the present limitations in deducing the mass inflow rates. This redshift dependence is similar to that inferred in star formation histories (or, more directly, in rest-frame ultraviolet light densities) where slopes over the  $z = 0 - 1$  interval have measured values in the range 1.5 to 4 (Lilly et al. 1996; Cowie, Songaila, & Barger 1999; G. Wilson, et al., in preparation).

We integrate the maximal accretion rate density from  $z = 0$  to  $z = 3$  to obtain a current black hole mass density,  $\rho_{BH} = 6 \times 10^{-35} \text{ g cm}^{-3}$ . This density can be compared to the spheroidal mass density of  $10^{-32} \text{ g cm}^{-3}$ , which is accurate to about a multiplicative factor of 2 (Cowie 1988; Fukugita et al. 1998). The ratio  $\rho_{BH}/\rho_{SPH} = 0.006$  is reasonably consistent with the black hole-bulge mass relation  $M_{BH} = 0.001 - 0.002 M_{bulge}$  found locally (e.g., Wandel 1999; Ferrarese & Merritt 2000; Gebhardt et al. 2000).

## 8. SUMMARY

The bulk of the hard X-ray background has already been resolved by deep *Chandra* surveys. In this paper we have presented follow-up multiwavelength studies of the AGN sources that comprise the background to ascertain their nature. By combining datasets from our previous studies of the CDF-N and SSA13 fields with new results on the A370 cluster field, we have amassed a large sample of 69 hard X-ray sources, of which 45 now have redshifts. With our optical, near-infrared, and 20 cm images of the fields, we have made a general analysis of AGN accretion phenomena. Our principal findings are as follows:

(i) About 4% of the  $> L^*$  galaxy population is X-ray luminous at any time, and hence the average duration of supermassive black hole accretion is about half a Gyr. Accretion activity might occur over this long a period in all galaxies, or some galaxies might be active for much longer periods while others are completely inactive.

(ii) We determined the X-ray, optical, and FIR luminosities of the hard X-ray sources. We then estimated the mass inflow rates onto the supermassive black holes, assuming a canonical radiative efficiency  $\epsilon = 0.1$ . We determined maximal inflow rates using  $L_{BOL} = L_{FIR} + L_{OPT} + L_X$  (this assumes the dominant component,  $L_{FIR}$ , is entirely due to reradiation of AGN light) and minimal rates using only the bolometric X-ray luminosities. These estimates differ by about a multiplicative factor of 20. Over the range  $z = 0.1$  to  $z = 1$ ,  $\log \dot{M}_{BH}$  increases approximately linearly with redshift. Above  $z = 1$ ,  $\log \dot{M}_{BH}$  flattens with redshift with a substantial scatter that may be due to a range of efficiencies,  $\epsilon$ , or to differences in the luminosities; the absence of sources at  $z > 1$  with  $\log \dot{M}_{BH} < 0.1$  is likely a selection effect. The maximal mass inflow rates increase from  $\sim 0.01 M_{\odot} \text{ yr}^{-1}$  at  $z \lesssim 0.5$  up to  $\sim 10 M_{\odot} \text{ yr}^{-1}$  at  $z \gtrsim 1$ .

(iii) We estimated the accretion rate density,  $d\rho_{BH}/dt$ , versus redshift. The time history of the accretion rate density seems to fall roughly as  $(1+z)^3$ . This is a similar dependence to that inferred in star formation histories. For the maximal ARD, the integrated value is  $\rho_{BH} = 6 \times 10^{-35} \text{ g cm}^{-3}$ , which is reasonably consistent with the local black hole mass relation combined with the estimated spheroidal density.

AJB acknowledges support from NASA through Hubble Fellowship grant HF-01117.01-A awarded by the Space Telescope Science Institute, which is operated by the Association of Universities for Research in Astronomy, Inc., for NASA under contract NAS 5-26555. We gratefully acknowledge support from NSF grants AST-0084847 (AJB) and AST-0084816 (LLC), NSF CAREER award AST-9983783 (WNB), NASA contracts NAS 8-37716 (MWB) and NAS 8-38252 (GPG, PI), NASA GSRP grant NGT 5-50247 and the Pennsylvania Space Grant Consortium (AEH).

## REFERENCES

Barger, A. J., Cowie, L. L., Trentham, N., Fulton, E., Hu, E. M., Songaila, A., & Hall, D. 1999a, AJ, 117, 102  
 Barger, A. J., Cowie, L. L., Smail, I., Ivison, R. J., Blain, A. W., & Kneib, J.-P. 1999b, AJ, 117, 2656  
 Barger, A. J., Cowie, L. L., & Richards, E. A. 2000, AJ, 119, 2092  
 Barger, A. J., Cowie, L. L., Mushotzky, R. F., & Richards, E. A. 2001a, AJ, 121, 662 (B01)  
 Bautz, M. W., Malm, M. R., Baganoff, F. K., Ricker, G. R., Canizares, C. R., Brandt, W. N., Hornschemeier, A. E., & Garmire, G.P. 2000, ApJ, 543, L119  
 Brandt, W. N., et al. 2001a, AJ, in press, (astro-ph/0102411)  
 Brandt, W. N., et al. 2001b, AJ, submitted  
 Carilli, C. L. & Yun, M. S. 2000, ApJ, 530, 618  
 Cohen, J. G., Hogg, D. W., Blandford, R., Cowie, L. L., Hu, E., Songaila, A., Shopbell, P., & Richberg, K. 2000, ApJ, 538, 29  
 Coleman, G. D., Wu, C.-C., & Weedman, D. W. 1980, ApJS, 43, 393  
 Condon, J. J. 1992, ARA&A, 30, 575  
 Cowie, L. L., Gardner, J. P., Hu, E. M., Songaila, A., Hodapp, K.-W., & Wainscoat, R. J. 1994, ApJ, 434, 114  
 Cowie, L. L., Songaila, A., Hu, E. M., & Cohen, J. G. 1996, AJ, 112, 839  
 Cowie, L. L., Songaila, A., & Barger, A. J. 1999, AJ, 118, 603  
 Cowie, L. L., et al. 2001, ApJ, 551, L9  
 Crawford, C. S., Fabian, A. C., Gandhi, P., Wilman, R. J., & Johnstone, R. M. 2001, MNRAS, submitted, (astro-ph/0005242)  
 Ferrarese, L. & Merritt, D. 2000, ApJ, 539, L9  
 Garmire, G. P., et al. 2001, ApJ, submitted

Gebhardt, K. et al. 2000, ApJ, 539, L13  
 Geller, M. J., et al. 1997, AJ, 114, 2205  
 Giacconi, R., et al. 2000, ApJ, in press, (astro-ph/0007240)  
 Hasinger, G., et al. 2001, A&A, 365, L45  
 Hodapp, K.-W. et al. 1996, NewA, 1, 177  
 Hornschemeier, A. E., et al. 2000, ApJ, 541, 49  
 Hornschemeier, A. E., et al. 2001, ApJ, in press, (astro-ph/0101494) (H01)  
 Ivison, R. J., Smail, I., Le Borgne, J.-F., Blain, A. W., Kneib, J.-P., Bézecourt, J., Kerr, T. H., & Davies, J. K. 1998, MNRAS, 298, 583  
 Kauffmann, G. & Haehnelt, M. 2000, MNRAS, 311, 576  
 Lilly, S. J., Tresse, L., Hammer, F., Crampton, D., & Le Fèvre, O. 1995, ApJ, 455, 108  
 Lilly, S. J., LeFèvre, O., Hammer, F., & Crampton, D. 1996, ApJ, 460, L1  
 Lin, H., Kirshner, R. P., Shectman, S. A., Landy, S. D., Oemler, A., Tucker, D. L., & Schechter, P. L. 1996, ApJ, 464, 60  
 Mushotzky, R. F., Cowie, L. L., Barger, A. J., & Arnaud, K. A. 2000, Nature, 404, 459  
 Oke, J. B., et al. 1995, PASP, 107, 375  
 Richards, E. A. 2000, ApJ, 533, 611  
 Schmidt, M., et al. 1998, A&A, 329, 495  
 Soucail, G., Kneib, J.-P., Bézecourt, J., Metcalfe, L., Altieri, B., & Le Borgne, J.-F. 1999, A&A, 343, L70  
 Tozzi, P., et al. 2001, ApJ, submitted, (astro-ph/0103014)  
 Wandel, A. 1999, ApJ, 519, L39

TABLE 1  
HARD X-RAY SOURCES IN THE A370 FIELD

#	RA(2000)	Dec(2000)	$f(2 - 7 \text{ keV})$ ( $10^{-15} \text{ erg cm}^{-2} \text{ s}^{-1}$ )	$f(0.5 - 2 \text{ keV})$ ( $10^{-16} \text{ erg cm}^{-2} \text{ s}^{-1}$ )	$HK'$	$I$	$R$	$V$	$z$	$\Delta\theta$ (arcsec)	$S(20\text{cm})$ ( $\mu\text{Jy}$ )
0	2 40 06.72	-1 36 56.2	$2.9 \pm 0.9$	$22.8 \pm 3.3$	...	18.6	19.8	...	0.421 <sup>n</sup>	0.6	30
1	2 40 04.76	-1 38 11.6	$5.7 \pm 1.5$	...	...	23.4	...	...	...	1.4	182
2	2 40 00.86	-1 33 13.2	$4.4 \pm 1.2$	$10.5 \pm 2.3$	17.6	20.1	21.5	22.3	0.730 <sup>n</sup>	0.5	25
3	2 40 00.25	-1 32 34.1	$4.4 \pm 1.2$	$22.6 \pm 3.3$	...	22.1	23.0	23.6	1.650 <sup>b</sup>	0.3	< 20
4	2 39 58.98	-1 35 48.9	$11.2 \pm 1.8$	$45.3 \pm 4.7$	18.3	20.0	20.6	21.0	1.603 <sup>b</sup>	0.3	< 20
5	2 39 58.62	-1 32 59.9	$6.5 \pm 1.4$	$26.1 \pm 3.6$	18.8	23.0	24.2	24.8	...	0.4	29
6	2 39 58.14	-1 32 36.1	$3.7 \pm 1.1$	...	...	23.0	24.1	24.8	...	0.3	29
7	2 39 57.92	-1 38 52.5	$2.8 \pm 1.0^a$	...	...	21.7	...	...	0.731 <sup>n</sup>	0.8	116
8	2 39 57.83	-1 37 05.9	$2.4 \pm 0.9$	$13.5 \pm 2.6$	...	23.1	...	...	0.688 <sup>n</sup>	0.4	39
9	2 39 57.74	-1 36 04.6	$2.5 \pm 0.9$	...	18.4	20.8	21.8	22.8	0.474 <sup>h</sup>	0.4	< 20
10	2 39 57.17	-1 32 59.4	$5.1 \pm 1.3$	...	15.8	18.3	19.3	20.4	0.360 <sup>n</sup>	0.2	28
11 <sup>c</sup>	2 39 56.59	-1 34 26.6	$28.3 \pm 2.9$	$9.5 \pm 2.5$	16.8	19.6	20.9	21.7	1.060 <sup>h</sup>	0.3	296
12 <sup>d</sup>	2 39 51.83	-1 35 58.5	$5.4 \pm 1.3$	...	18.4	21.2	21.9	22.6	2.800 <sup>h</sup>	0.4	124
13	2 39 49.66	-1 38 45.4	$5.6 \pm 1.4$	$89.0 \pm 6.7$	...	20.9	...	...	1.512 <sup>b</sup>	0.5	52
14	2 39 49.22	-1 36 57.3	$13.1 \pm 2.0$	$65.5 \pm 5.7$	...	21.3	21.8	22.2	3.268 <sup>b</sup>	0.4	28

NOTE.— <sup>a</sup>Flux based on counts measured in a  $2''$  radius aperture. <sup>c</sup>Flux and magnitudes uncorrected for magnification by a factor of 2.1. <sup>d</sup>Flux and magnitudes uncorrected for magnification by a factor of 2.4; spectrum from Ivison et al. (1998). In column (10) the superscript “b” denotes sources with broad emission lines, “h” denotes sources with high ionization lines, and “n” denotes a “normal” galaxy spectrum. Source 13 coordinates are the means of the positions in the soft and hard bands. For source 11, which appears to be a radio jet, we have used the flux associated with a bright peak near the X-ray source, which may be considered an upper limit on the flux associated with the object. For source 12 we have used the radio flux at the X-ray position, excluding emission which appears to arise in the neighboring optical emission-line object. Source 1 appears to be a radio double, and the radio flux may not be directly associated with the X-ray source.

TABLE 2  
SUPPLEMENTAL SOFT X-RAY SOURCES IN THE A370 FIELD

#	RA(2000)	Dec(2000)	$f(0.5 - 2 \text{ keV})$ ( $10^{-16} \text{ erg cm}^{-2} \text{ s}^{-1}$ )	$z$	$S(20\text{cm})$ ( $\mu\text{Jy}$ )
S0	2 40 10.60	-1 37 04.7	$3.1 \pm 1.2$	3.025	< 20
S1	2 40 06.17	-1 34 01.0	$6.7 \pm 1.8$	0.553	40
S2	2 40 05.30	-1 36 31.2	$8.8 \pm 2.1$	...	< 20
S3	2 40 03.70	-1 39 43.1	$4.1 \pm 1.5$	...	< 20
S4	2 40 02.16	-1 35 09.0	$5.1 \pm 1.6$	...	37
S5	2 40 00.92	-1 35 16.2	$6.2 \pm 1.8$	0.380	< 20
S6	2 40 00.12	-1 31 58.1	$7.0 \pm 1.9$	...	< 20
S7	2 39 58.74	-1 37 50.4	$5.2 \pm 1.6$	...	< 20
S8	2 39 58.64	-1 33 09.2	$22.5 \pm 3.3$	1.303	21
S9	2 39 56.35	-1 31 36.9	$28.5 \pm 3.8$	0.026	883
S10	2 39 54.64	-1 32 33.5	$199. \pm 10.$	0.045	358
S11	2 39 52.93	-1 34 26.2	$8.6 \pm 3.1$	...	< 20
S12	2 39 47.53	-1 35 12.2	$7.7 \pm 2.1$	1.605	< 20
S13	2 39 40.30	-1 34 31.2	$11.6 \pm 2.5$	0.423	76

TABLE 3  
HARD X-RAY SOURCES IN THE CDF-N FIELD

#	CXO HDFN Name (J2000)	$f(2 - 7 \text{ keV})$ ( $10^{-15} \text{ erg cm}^{-2} \text{ s}^{-1}$ )	$f(0.5 - 2 \text{ keV})$ ( $10^{-15} \text{ erg cm}^{-2} \text{ s}^{-1}$ )	$HK'$	$I$	$V$	$B$	$z$	$S(20\text{cm})$ ( $\mu\text{Jy}$ )
0	123615.9+621515	2.39	0.19	$> 21.5$	24.4	26.1	$> 26.1$	...	54
1	123616.0+621107	12.10	1.05	21.1	24.4	$> 26.4$	$> 26.1$	...	$< 23$
2	123617.0+621011	3.31	1.87	18.7	21.7	24.0	24.3	0.845 <sup>n</sup>	62
3	123618.0+621635	10.40	6.32	18.0	19.9	21.4	22.3	0.679 <sup>n</sup>	47
4	123618.5+621115	7.25	7.66	18.2	21.0	22.0	21.8	1.022 <sup>b</sup>	$< 23$
5	123619.1+621441	1.42	1.34	21.1	24.3	25.2	$> 26.1$	...	$< 23$
6	123621.3+621109	1.16	...	18.3	21.9	26.1	25.6	1.014 <sup>n</sup>	53
7	123622.6+621028	2.18	1.09	20.9	24.7	25.9	$> 26.1$	...	$< 23$
8	123622.9+621527	8.81	7.69	18.7	20.0	20.5	20.4	2.590 <sup>b</sup>	$< 23$
9	123627.5+621026	3.94	0.25	20.4	22.8	25.2	25.9	0.761 <sup>n</sup>	$< 23$
10	123627.7+621158	1.09	...	$> 21.5$	23.7	25.7	$> 26.1$	...	$< 23$
11	123629.0+621046	1.57	...	18.9	22.8	25.8	$> 26.1$	1.013 <sup>n</sup>	81
12	123629.2+621613	1.88	...	18.3	20.4	23.4	23.8	0.848 <sup>n</sup>	$< 23$
13	123635.6+621424	1.84	0.36	19.4	22.9	23.8	24.1	2.005 <sup>h</sup>	88
14	123636.6+621347	2.44	2.94	19.0	21.1	22.1	22.6	0.957 <sup>h</sup>	$< 23$
15	123642.2+621711	1.50	0.97	21.4	23.7	25.2	25.8	2.724 <sup>b</sup>	$< 23$
16	123642.2+621545	1.62	0.41	18.1	21.2	23.3	24.2	0.857 <sup>h</sup>	150
17	123646.3+621404	17.48	2.82	18.2	21.0	22.8	23.7	0.961 <sup>h</sup>	179
18	123646.6+620857	1.01	...	19.2	23.0	$> 26.4$	$> 26.1$	...	$< 23$
19	123651.2+621051	1.72	...	19.6	23.3	$> 26.4$	$> 26.1$	...	$< 23$
20 <sup>a</sup>	123651.7+621221	2.60	0.18	$> 22.6$	$> 25.3$	22.9	23.6	...	49
21	123658.8+621435	5.47	2.48	17.9	20.4	22.5	23.0	0.678 <sup>n</sup>	$< 23$
22	123702.7+621543	16.03	5.41	17.2	19.2	21.0	21.0	0.514 <sup>n</sup>	$< 23$
23	123704.6+621652	1.15	1.18	18.2	20.1	21.4	22.3	0.377 <sup>h</sup>	$< 23$
24	123704.8+621601	4.91	2.91	$> 21.5$	25.2	$> 26.4$	$> 26.1$	...	$< 23$
25	123706.8+621702	14.38	14.72	18.0	19.6	20.0	20.1	1.020 <sup>b</sup>	$< 23$
26	123713.7+621424	1.00	...	18.5	21.2	23.2	24.1	0.475 <sup>n</sup>	$< 23$
27	123714.1+620916	1.60	0.84	20.2	24.0	26.0	26.0	...	$< 23$
28	123714.8+621617	1.18	0.66	20.4	23.3	24.0	24.3	...	$< 23$
29	123715.9+621213	1.15	...	19.2	22.3	25.0	25.5	1.019 <sup>h</sup>	$< 23$
30	123716.7+621733	14.56	4.57	18.8	22.2	24.3	24.9	1.147 <sup>h</sup>	346
31	123724.0+621304	2.20	0.27	20.4	23.6	25.2	25.3	...	$< 23$
32	123724.3+621359	1.55	...	20.9	24.1	25.8	25.5	...	$< 23$
33	123725.0+620856	2.03	0.41	18.7	22.2	25.6	$> 26.1$	...	90

NOTE.— <sup>a</sup>X-ray coordinate offset from bright galaxy at  $z = 0.401$  is  $1.2''$ ; radio coordinate offset from bright galaxy is  $1.4''$ . In column (10) the superscript “b” denotes sources with broad emission lines, “h” denotes sources with high ionization lines, and “n” denotes a “normal” galaxy spectrum.

TABLE 4  
OPTICAL TO HARD X-RAY FLUXES

Range ( $10^{-15} \text{ erg cm}^{-2} \text{ s}^{-1}$ )	# Sources	$\langle f(2 - 7 \text{ keV}) \rangle$ ( $10^{-15} \text{ erg cm}^{-2} \text{ s}^{-1}$ )	$\langle I \rangle$	median $I$
1–2	19	1.4	21.8	23.0
2–5	27	3.0	19.0	22.8
$> 5$	23	11.3	19.8	20.5

TABLE 5

SPECTRAL CLASSES FOR THE A370, CDF-N, AND SSA13 HARD X-RAY SAMPLES

Class	A370	CDF-N	SSA13	Summed
Broad Line	4	4	2	10
High Ionization	3	7	5	15
‘Normal’	5	9	6	20
Unidentified $I \leq 23.5$	3	4	0	7
Unidentified $I > 23.5$	0	10	7	17

TABLE 6  
LUMINOSITIES FOR THE A370 AND CDF-N HARD X-RAY SAMPLES

Number	$z$	$L_{HX}$ ( $10^{42}$ ergs s $^{-1}$ )	$L_{OPT}$ ( $10^{42}$ ergs s $^{-1}$ )	$L_{FIR}$ ( $10^{42}$ ergs s $^{-1}$ )
A370				
0	0.421	2.1	...	170
1	2.000	180	...	39000
2	0.730	12	...	510
3	1.650	89	1400	< 2700
4	1.603	210	12000	< 2600
5	2.000	210	1100	6200
6	2.000	120	1200	6200
7	0.731	7.8	...	2400
8	0.688	5.7	...	690
9	0.474	2.4	...	< 150
10	0.360	2.6	...	110
11	1.060	92	...	6900
12	2.800	160	6700	24000
13	1.512	92	...	5800
14	3.268	1400	...	18000
CDF-N				
0	2.000	77	340	12000
1	2.000	390	320	< 4900
2	0.845	13	160	1800
3	0.679	24	610	810
4	1.022	45	1800	< 1000
5	2.000	46	430	< 4900
6	1.014	7.1	45	2300
7	2.000	70	280	< 4900
8	2.590	530	38000	< 8900
9	0.761	12	38	< 520
10	2.000	35	610	< 4900
11	1.013	9.6	46	3600
12	0.848	7.5	260	< 670
13	2.005	60	1600	19000
14	0.957	13	1800	< 880
15	2.724	100	1600	< 9900
16	0.857	6.6	210	4400
17	0.961	94	400	7000
18	2.000	33	900	< 4900
19	2.000	56	720	< 4900
20	2.000	84	310	10000
21	0.678	13	210	< 390
22	0.514	19	630	< 210
23	0.377	0.66	110	< 100
24	2.000	160	180	< 4900
25	1.020	90	10000	< 1000
26	0.475	1.0	28	< 170
27	2.000	52	460	< 4900
28	2.000	38	1100	< 4900
29	1.019	7.2	200	< 1000
30	1.147	120	240	20000
31	2.000	71	720	< 4900
32	2.000	50	450	< 4900
33	2.000	66	1900	19000

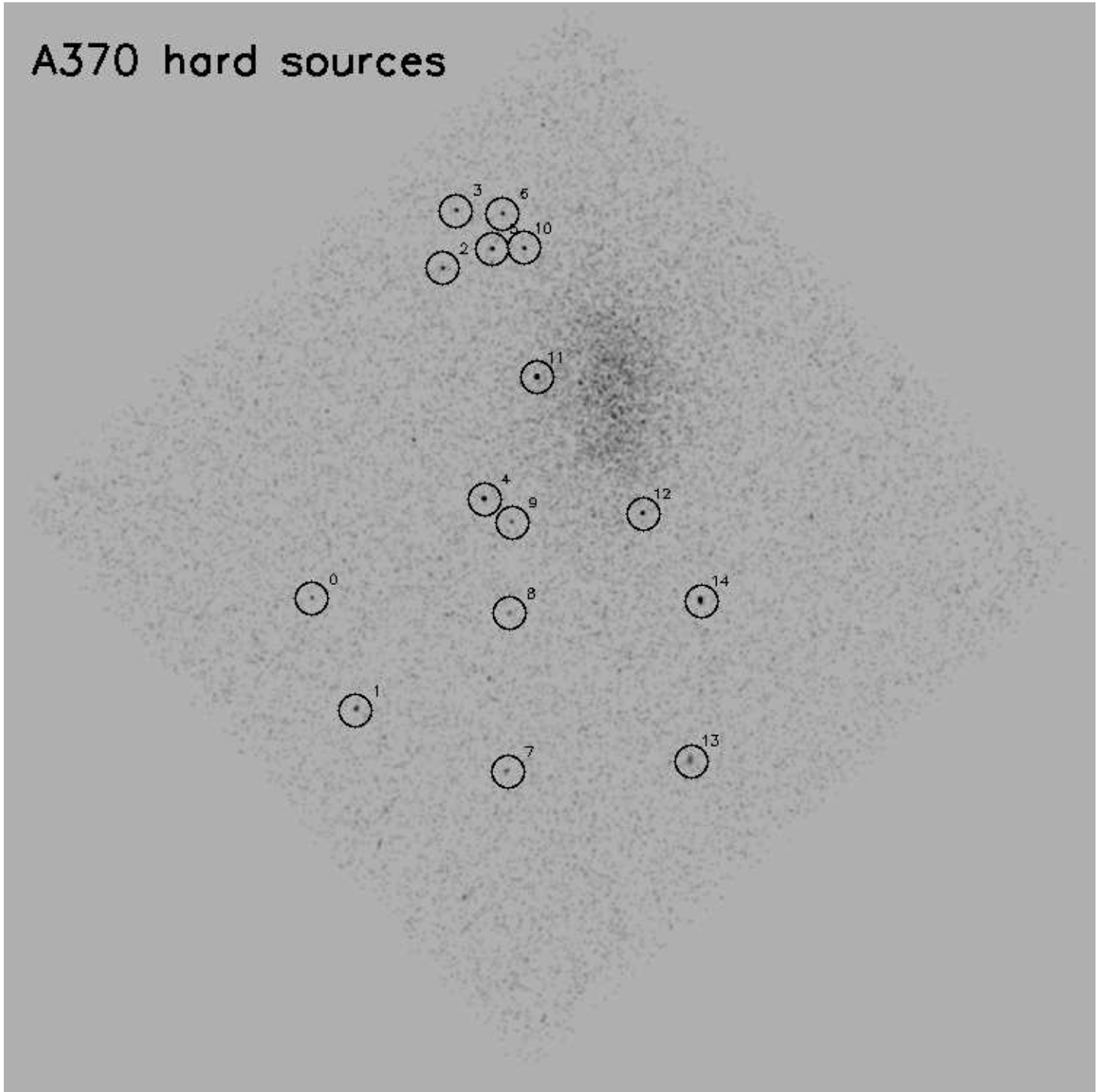


FIG. 1.— *Chandra* hard X-ray image of the A370 field. The 15 significant hard X-ray source positions are identified by the small circles. The X-ray image has been smoothed with a 2.5'' boxcar smoothing to allow the X-ray sources to be clearly seen.

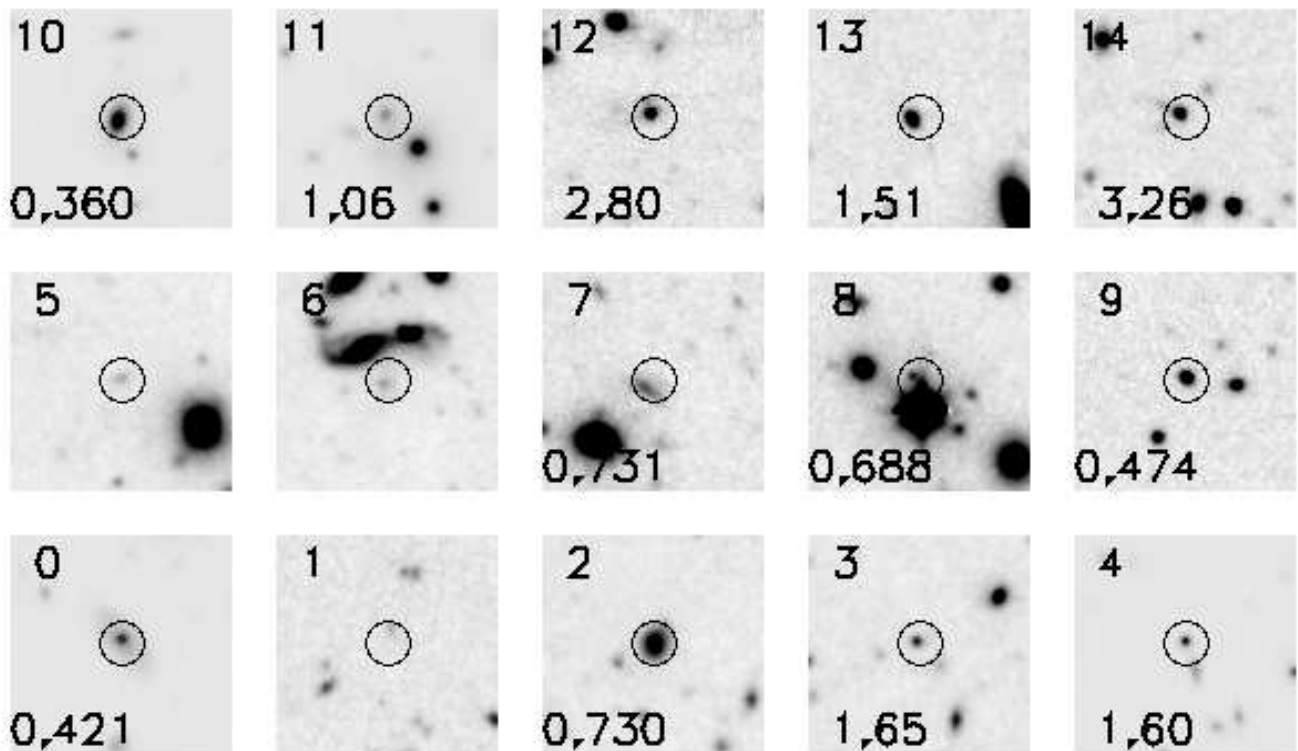


FIG. 2.—  $9'' \times 9''$   $I$ -band thumbnail images of the A370 hard X-ray sources listed in Table 1. The images are from ultradepth data obtained with LRIS on Keck. The identification numbers are as in Table 1. A circle of  $1.5''$  radius, typical of the maximum positional uncertainty, is superimposed on each thumbnail. Redshifts, where available, are given in the lower left-hand corners of the thumbnails. North is up and East is to the left. For the more luminous objects we have shown the images at higher surface brightness to allow the positions of the objects with respect to the centers of the galaxies to be seen.

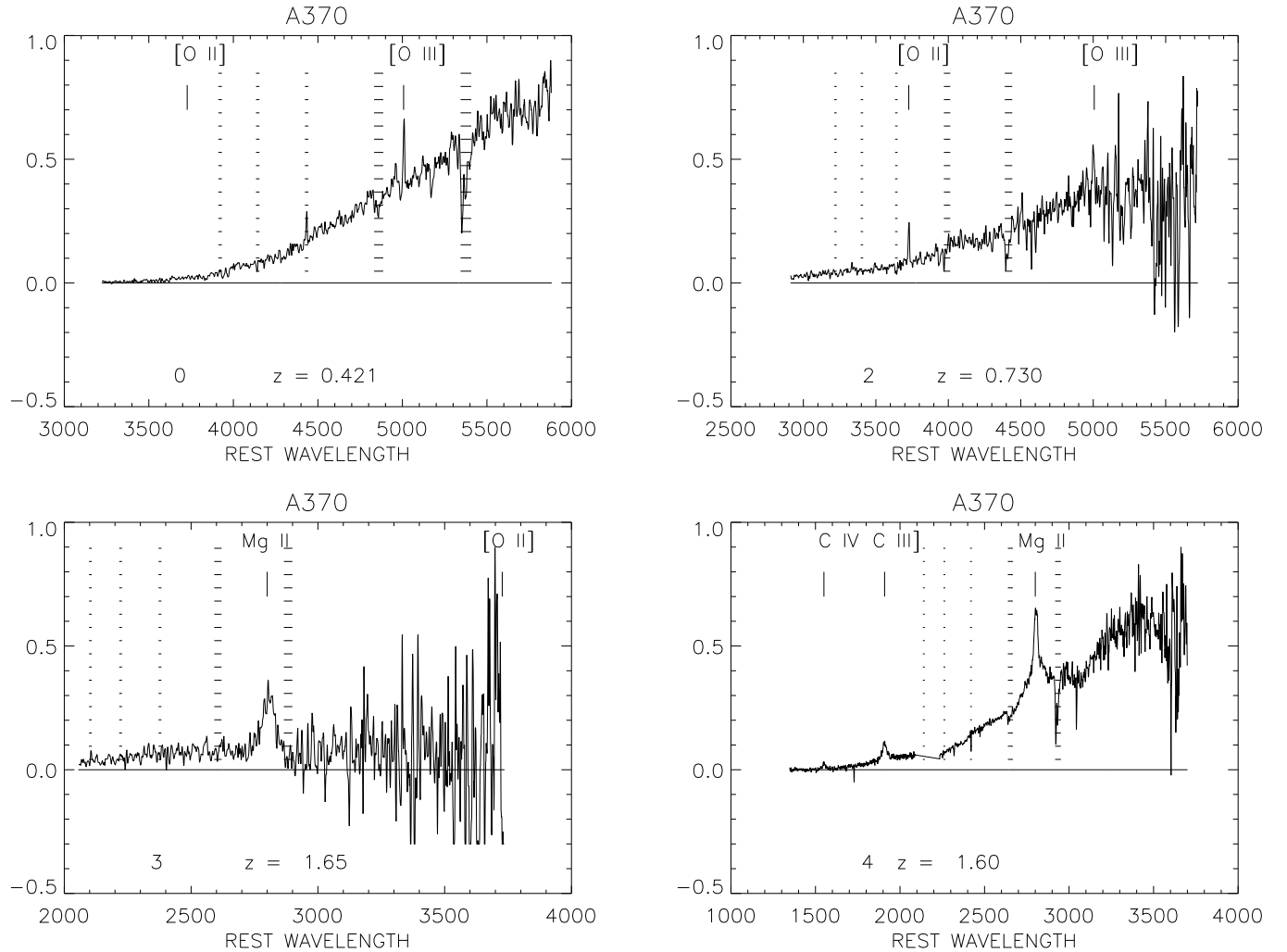


FIG. 3.— Keck LRIS spectra of the A370 hard X-ray sources with secure redshift identifications (except source 12). The spectra are shown in the rest frame with source number and the measured redshift at the bottom of the frame. Dashed lines mark strong atmospheric absorption or emission features.

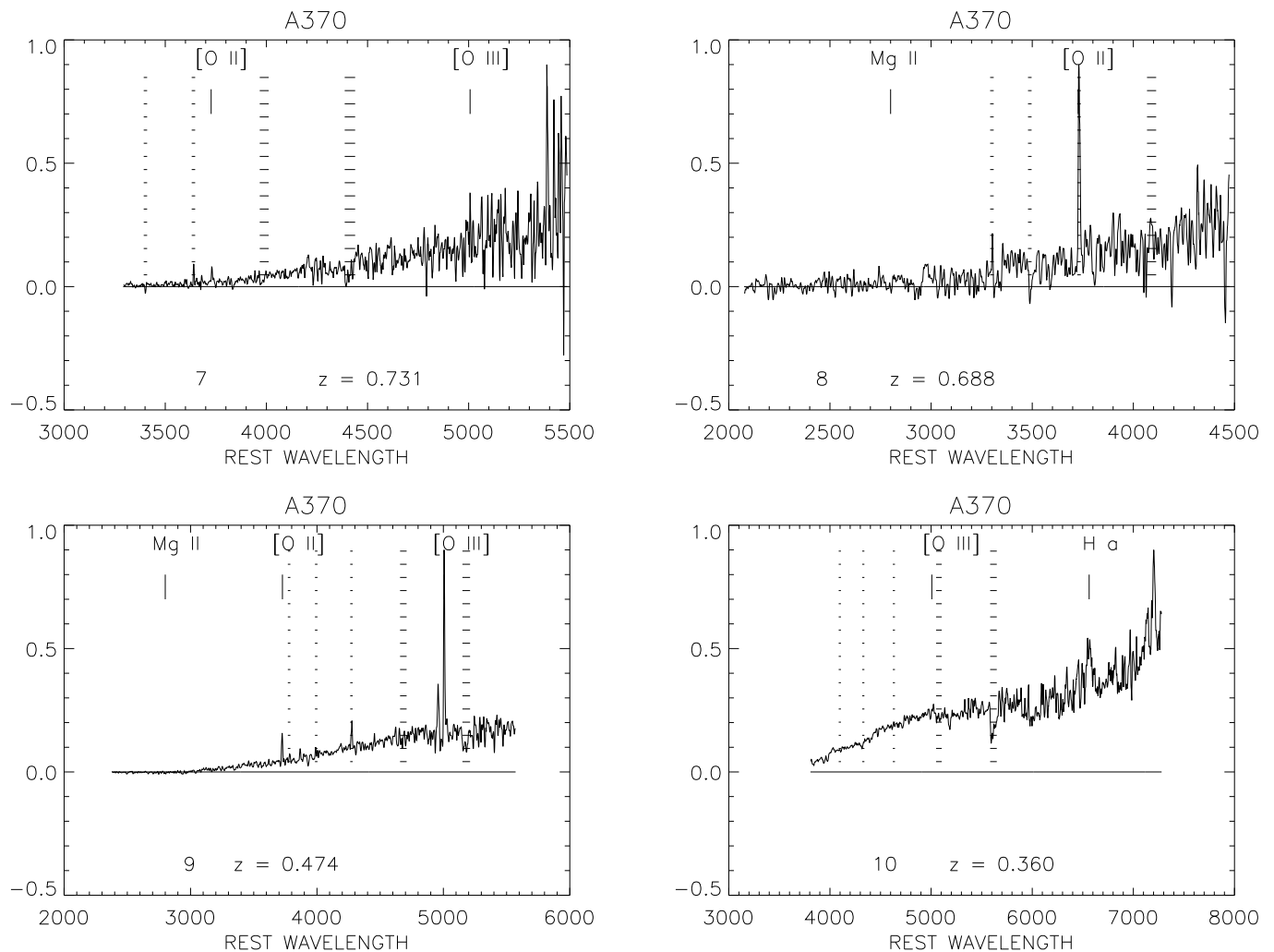


FIG. 3.—

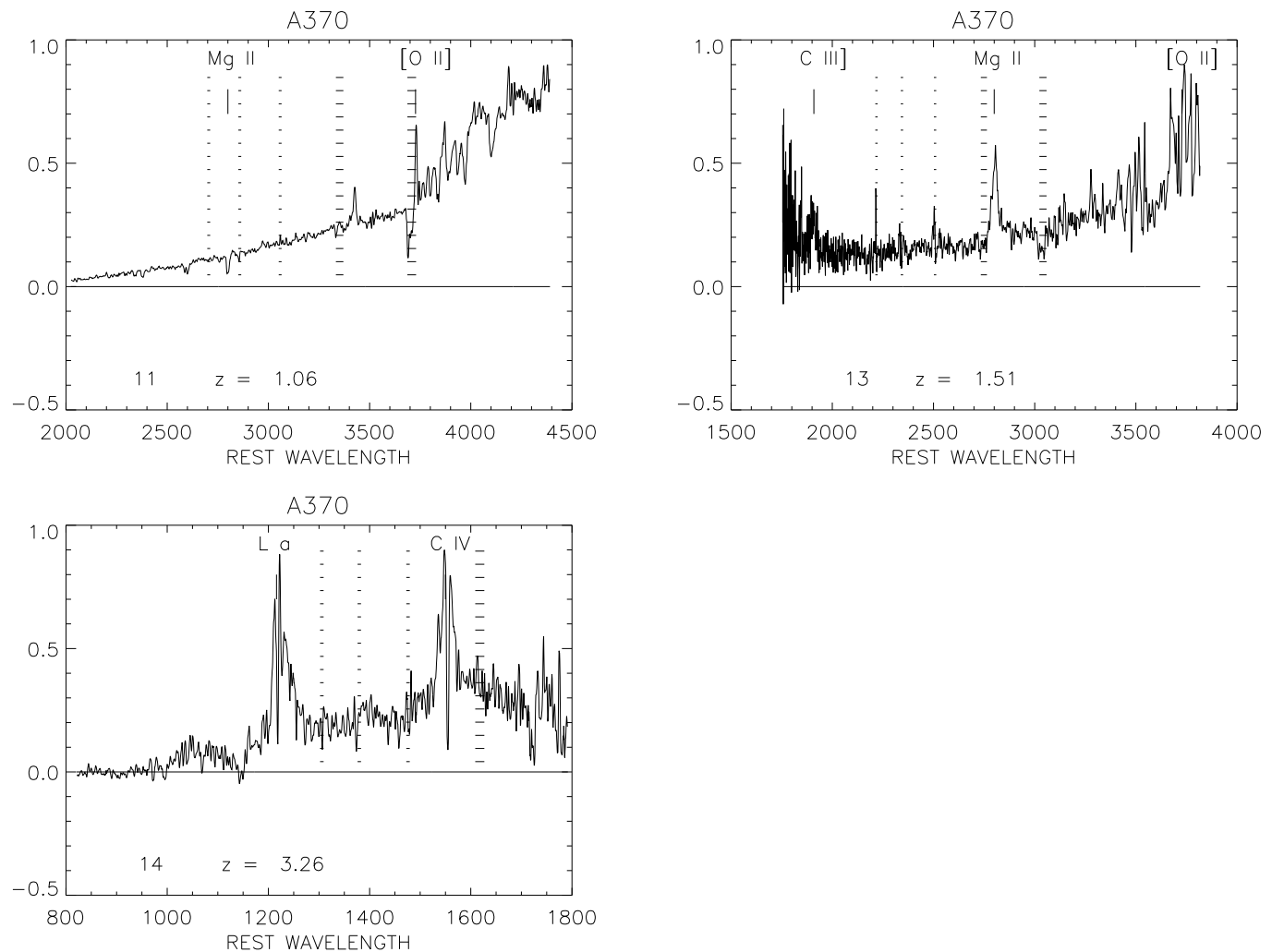


FIG. 3.—